



Dual-tandem phased array method for imaging of near-vertical defects in narrow-gap welds

Ewan Nicolson^{a,*}, Ehsan Mohseni^a, Sumana^{a,b}, David Lines^a, Gareth Pierce^a, Charles N. MacLeod^a

^a University of Strathclyde, 16 Richmond St, Glasgow, G1 1XQ, UK

^b PEAK NDT, 1 Enterprise Way, Derby, DE21 4BB, UK

ARTICLE INFO

Keywords:

Ultrasonics
Weld inspection
Narrow-gap welding
Total focusing method (TFM)
Phased array ultrasonic testing (PAUT)

ABSTRACT

Near-vertical flaws in thick-section narrow-gap welds are notoriously difficult to detect and size using traditional Phased Array Ultrasonic Testing (PAUT) techniques. Self-tandem shear inspection has been considered for detection but lacks appropriate full weld sensitivity. The dual-tandem phased array inspection method is proposed to enable multi-mode Total Focusing Method (TFM) pulse-echo imaging with longitudinal through-transmission inspection, by introducing a second, opposite-facing probe on the far weld side. Pulse-echo and through-transmission datasets are obtained in a single Full Matrix Capture (FMC) acquisition, for each weld side. Analysis of the optimum Probe Centre Spacing (PCS) based upon image sensitivity suggests that a spacing corresponding to a longitudinal beam crossover at 2/3 sample thickness provides greatest weld coverage. Testing on near-vertical EDM notches in a 120 mm thick mock narrow-gap carbon steel sample has shown high sensitivity TFM imaging, at notch depths of 27.5 mm, 60 mm and 92.5 mm. Pitch-catch through-weld transmission imaging has exhibited tip-diffraction images with a Signal-to-Noise Ratio (SNR) of up to 17.3 dB. Pulse-echo imaging using multi-mode TFM has shown tip-diffraction and reflection with up to 19.2 dB and 34.8 dB SNR respectively. The possibility of image mixing by considering image defect response type has provided full 2D notch reconstruction. These results demonstrate the strength of the dual-tandem method in enhancing the detection reliability and detection of near-vertical defects in thick-section narrow-gap welds.

1. Introduction

The emergence of Phased Array Ultrasonic Testing (PAUT) technology to the Non-Destructive Testing (NDT) industry has dramatically changed the landscape of ultrasonic inspection capabilities. This is largely due to the flexible acquisition process and improved scanning efficiency that phased arrays can guarantee [1]. By manipulating time delays of electrical excitation pulses sent to individual piezoelectric elements in the phased array, ultrasonic phase delays can be induced, allowing resulting beams focussed and steered accordingly [2]. In turn, this has led to the rapid uptake and dependability of PAUT in NDT, in areas such as weld inspection [3], additive manufacturing [4,5], composite testing [6], and non-piezo wave generation such as laser induced phased arrays [7].

The ability to excite elements singularly or simultaneously in ultrasonic transmission and reception is a key enabler to Full Matrix Capture (FMC) acquisition. This allows delay-and-sum imaging algorithms to be

applied in post-processing, contrary to traditional PAUT which requires active beamforming during inspection [8]. There are a vast number of imaging algorithms available for post-process imaging of FMC datasets, which are practically inefficient to implement using traditional beamforming phased array techniques. These techniques include the wave-number algorithm [9], Phase Coherence Imaging (PCI) [10], and Inverse Wave field Extrapolation (IWEX) [11]. However, it is the Total Focusing Method (TFM) which is widely considered the 'gold standard' of the available post-processing imaging algorithms [12]. An amplitude-based delay-and-sum method, TFM provides synthetic focusing of the full array aperture in transmission and reception at every point in a discretised image region. This is performed by applying post-acquisition time delays to full matrix data and has been shown to provide high-resolution reconstruction and sensitivity to flaws [13,14].

Given the extensive focusing capabilities of the TFM algorithm in both transmission and reception, Time-of-Flight (ToF) maps are typically generated to efficiently provide the time delays required. A

* Corresponding author.

E-mail address: ewan.nicolson@strath.ac.uk (E. Nicolson).

<https://doi.org/10.1016/j.ndteint.2023.102808>

Received 28 November 2022; Received in revised form 13 January 2023; Accepted 23 January 2023

Available online 30 January 2023

0963-8695/© 2023 The Authors. Published by Elsevier Ltd. This is an open access article under the CC BY license (<http://creativecommons.org/licenses/by/4.0/>).

focused beam can be synthesised accordingly, and an amplitude value obtained from the FMC dataset at each point in the image. The ToF map depends upon the ultrasonic wave velocity of the given material, as well as refractive effects observed across velocity variations caused by changing elastic properties. The ability to calculate time delays in this manner lends itself to the Multi-Mode TFM (MM-TFM) algorithm [13]. This algorithm provides increased array adaptability to detection of planar-type defects, such as cracks and Lack-of-Sidewall-Fusion (LOSWF) flaws in weld inspection.

An open V-groove geometry is often used for standard bevel welds, such as that shown on the left of Fig. 1. V-groove welds are typically machined to a bevel angle between 20° and 45° . International standard BS EN ISO 13588:2019 [15] requires an inspection of this kind to ensure an incident beam within 6° of the bevel normal, and can typically be achieved using a sectorial scan, or shear half-skip (e.g. TT-TT) TFM. By solely considering shear waves in transmission and reception, an effective reflection can be obtained from a potential LOSWF defect positioned on the weld bevel.

However, narrow J-groove bevel geometries are commonly selected to conserve weld volume in thick section narrow-gap welds. Contrary to the large bevel angles associated with V-groove welds, narrow-gap grooves typically utilise angles from 2° to 6° . For this reason, LOSWF flaws manifest at near-vertical angles, and complicate the inspection procedure required to observe a consistent sensitivity for LOSWF detection. Traditional phased array methods can show improvement using the self-tandem 3T (TT-T) TFM image mode. The use of multi-mode self-tandem imaging has also been shown to be effective using FMC-TFM [16]. However, this relies on achieving a favourable reflected angle from the LOSWF flaw and can require several scan positions to cover the full weld area – particularly in thick-section components. The requirement for a maximum beam deviation of 6° on the bevel also becomes impractical and would require large probe offset distances to satisfy.

As the prominence of narrow-gap welding increases, the desire to develop an efficient and reliable inspection method for the testing of narrow-gap welding components is in high demand. This work attempts to address this issue by proposing a dual-tandem phased array inspection method. This method introduces a second, opposite facing array on the far weld side, designed to address the difficulty in the detection of near-vertical defects. The addition of a second probe not only ensures a consistent detection sensitivity from each weld side, but also introduces the ability to perform through-weld detection (see Fig. 2). By separating the transmission and reception across two probes, sensitivity to geometric effects - such as diffraction - can be increased, improving the likelihood of detection and reducing sizing errors associated with near-vertical defects. In addition to this, a wedge design balancing the transmission of both longitudinal and shear modes would allow the full benefit of multi-mode TFM to be exploited. Such a wedge would allow longitudinal through-transmission imaging, utilising diffraction effects,

while maintaining the ability to perform multi-mode pulse-echo imaging.

In recent years, the ability to combine welding and NDT processes at the point of manufacture has grown in demand. An in-process inspection approach enables flaws to be detected and corrected between weld passes, reducing rework, increasing manufacturing throughput, and schedule certainty. However, when considering in-process ultrasonic inspection, several key challenges - including partially-filled geometries, high temperature gradients and process interference - limit deployment. While traditional phased array techniques using high-temperature wheel probes [17,18] have shown promise in traditional open V-groove weld inspection, such approaches have not yet been considered for narrow-groove welding practices. Therefore, there is a requirement for the design of narrow-groove weld inspection processes for both fully-filled cold welds and partially-filled welds inspected in-process.

In this paper, the dual-tandem method is introduced and demonstrated as a method for the detection and inspection of near-vertical defects in cold thick section components mimicking fully-filled narrow-gap welds. Notches created using an Electrical Discharge Machining (EDM) process were placed within the samples to simulate the positioning expected from a LOSWF defect in a 2° narrow J-groove weld. It will be shown that this method can provide high sensitivity imaging of near-vertical flaws using multi-mode pulse-echo TFM and longitudinal through-transmission imaging. Furthermore, the possibility of image mixing will be explored, in order to visualise the full geometric extent of a defect in the two-dimensional image plane.

2. Methodology

In this paper, the process of determining the presence and geometry of a given defect begins with the acquisition of the full-matrix dataset. However, to acquire an FMC dataset in which beam energy is optimised to cover the full weld area, the probe position must be considered. Once one or more FMC frames are collected, the data can be processed, and ToF maps calculated, to form the necessary images to assess the presence and extent of potential flaws. This requires consideration of known weld geometries, to determine the correct imaging mode to select to maximise flaw sensitivity. Once images have been obtained, they can be observed separately, or 'mixed' to condense the information gathered.

In order to ensure the transmission and reception of both shear and longitudinal modes in a single acquisition, a numerical analysis of Snell's law was conducted to identify an optimised wedge angle for the probe assembly. This considered the ability of the assembly to transmit and receive longitudinal and shear modes in a single acquisition. The refraction angle of the resulting shear and longitudinal modes versus wedge angle were computed and displayed in Fig. 3.

From this study, a wedge angle of 20° was determined to provide a balance between increasing the longitudinal refraction angle towards

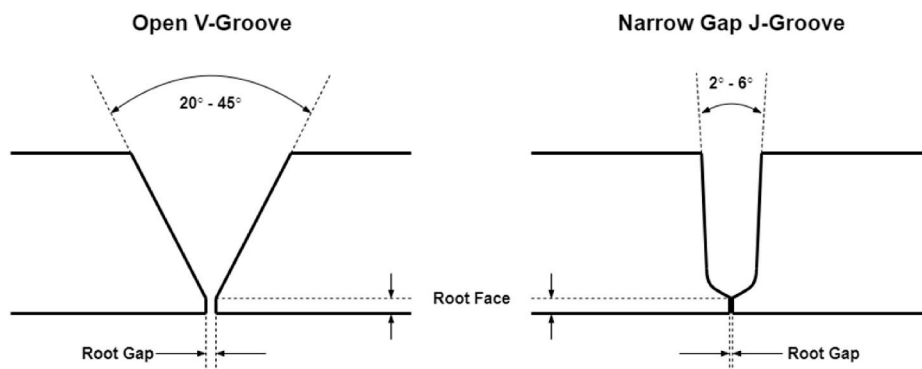


Fig. 1. Comparison of open V-groove weld geometry (left) and narrow-gap J-groove geometry (left).

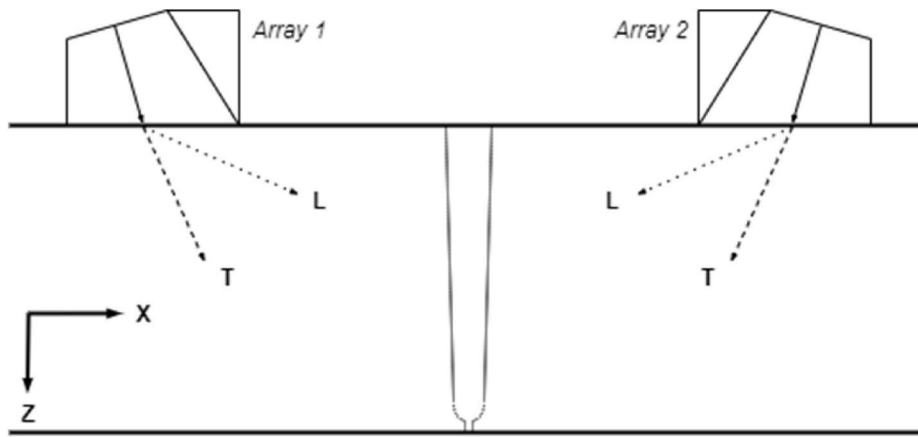


Fig. 2. Dual-tandem phased array configuration.

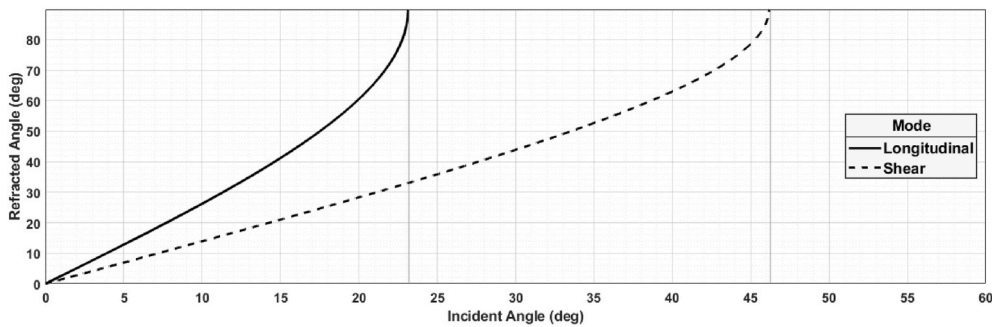


Fig. 3. Shear and longitudinal refraction angles at a Rexolite-Steel boundary as a function of incident angle.

the first critical angle and limiting the shear refraction angle. This provided refraction angles of 60° and 28° for longitudinal and shear waves respectively, across a Rexolite ($v_L^R = 2330 \text{ ms}^{-1}$) wedge to carbon steel ($v_L^S = 5930 \text{ ms}^{-1}$, $v_T^S = 3240 \text{ ms}^{-1}$) interface.

The equipment used throughout this work is therefore as follows.

- 5 MHz 64-element Olympus A32 arrays (0.50 mm pitch, 0.42 mm element width)
- 60LW Rexolite Olympus A32 wedges (20° angle)
- PEAK-NDT MicroPulse 6 128/256 channel array controller

The workflow of the imaging system proposed in this work is outlined in Fig. 4. The components highlighted will be discussed in the relative section, starting with the acquisition process, then ToF map calculation, TFM imaging algorithm, multi-view and multi-mode image mixing, and finally an image sensitivity calculation method.

2.1. FMC acquisition

With the inclusion of two phased array probes, the FMC acquisition process increases in complexity. Considering the two individual arrays as a single aperture, the full matrix dataset can be obtained at a size 4x greater than that for a single probe. For two arrays of N elements each, a dataset of $4N^2$ A-scans is obtained.

This dataset can be split into four sub-datasets of size N^2 , each of which will be referred to as an individual ‘view’ available to the system. An example of the full matrix dataset obtained can be seen in Fig. 5. This assumes that elements 1 to N belong to the left array, and elements $N + 1$ to $2N$ to the right array (see Table 1).

This means that from a single acquisition, a full dataset containing the two pulse-echo and two through-transmission views can be collected, to be analysed with post-processing imaging techniques.

Throughout this work, consistent scan parameters were used in the

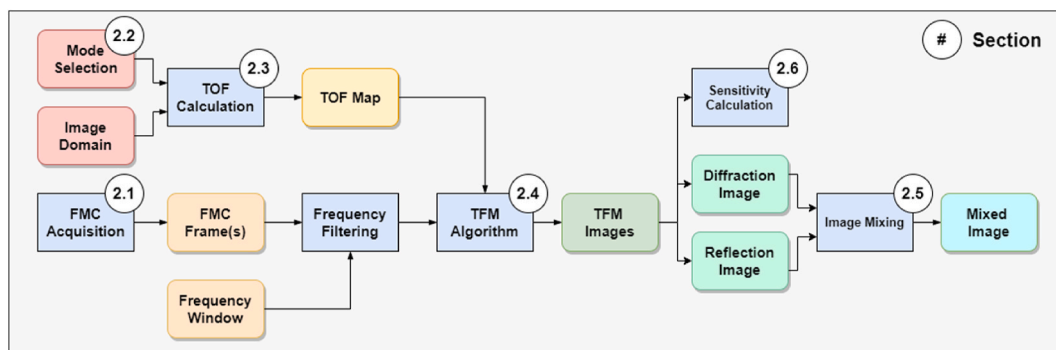


Fig. 4. Imaging system workflow.

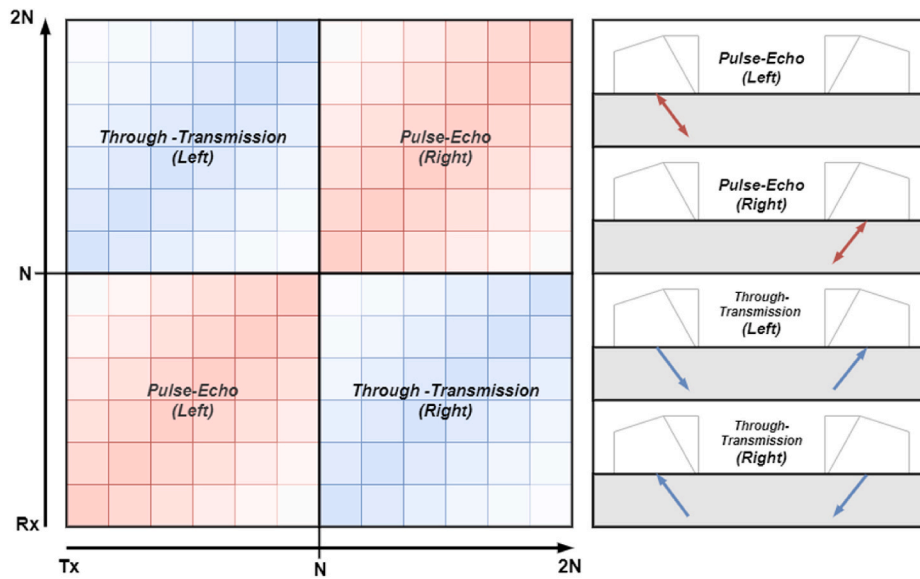


Fig. 5. Full matrix obtained from dual tandem FMC, showing four unique views.

Table 1
Element numbers for each dual-tandem view.

	Direction	N_{Tx}			N_{Rx}		
Pulse-Echo	Left	1	-	64	1	-	64
	Right	65	-	128	65	-	128
Through-Transmission	Left	1	-	64	65	-	128
	Right	65	-	128	1	-	64

FMC acquisition process. These are detailed in Table 2. The data acquisition was conducted using software designed in National Instruments LabVIEW [19], to interface with the PEAK NDT array controller. Data was saved in a HDF5 Multi-Frame Matrix Capture (MFMC) file format [20], and subsequently processed in MATLAB-based imaging software.

2.2. Mode selection

Six imaging modes were chosen with a mix of mode converted and non-mode converted imaging modes, to allow an understanding of the imaging performance of various modes in both pulse-echo and through-transmission views.

Six pulse-echo modes were selected, including the direct longitudinal mode (L-L) and five self-tandem modes. For through-transmission imaging, only the direct longitudinal mode was used. Of the eight possible self-tandem modes, these five were chosen to provide a variety of mode conversion and propagation angles. As the focus of this work is the enabling and improving of diffraction sensitivity to near-vertical defects, five of the six modes were chosen with a longitudinal mode incident or reflection/diffracted from a defect. A final TT-T mode was also selected to provide comparison to the standard shear self-tandem weld inspection technique. These are detailed in Fig. 6.

Table 2
FMC acquisition parameters.

	Unit	Value	
PRF	Hz	1	
Sample Frequency	MHz	25	
Excitation	V	200	
Gain	dB	60	
Time Window	μs	64	224

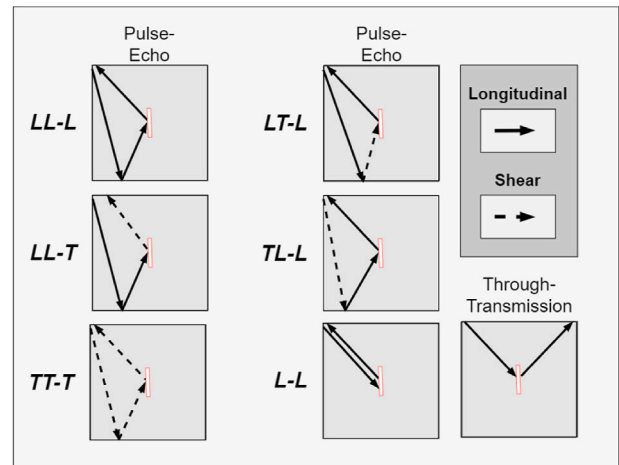


Fig. 6. Six modes selected for multi-mode imaging.

2.3. ToF mapping

To accurately extract the correct amplitude values at each pixel in the discretised image region, a ToF value must be calculated for each array element in the system, and for each image mode. The result is a four dimensional array, of size $X \times Z \times N_T \times M$, where X and Z are the pixel counts along the x- and z-dimensions of the image domain, N_T is the total number of source elements in the system, and M is the number of image modes selected.

There are currently several ray-tracing methods to calculate the ToF maps. One such method is the generalised bisection method, which is a root-finding method for determining the optimum ray path through one or more boundaries [21,22]. This method is efficient when considering flat layers of homogenous material and assumes that refraction occurs only at a defined boundary. A more involved method of ToF mapping is the Multi-Stencil Fast Marching Method (MSFMM). This is an efficient path finding algorithm which continually computes a solution to the Eikonal equation [23–25]. This method defines a ToF value based upon an upwind difference scheme condition, allowing refractive effects to be accounted for at every grid point.

The result of the MSFMM is a numerical array containing a ToF map for each view - pulse-echo and through-transmission from each side - for

every element pair, for each mode. The ToF values generated by a single execution of this algorithm need only be run once and can be used to produce TFM images for any number of FMC frames which possess the same geometric setup, given that material properties can be assumed to remain consistent across each frame.

2.4. TFM algorithm

For a pixel position (x_i, z_j) on the TFM image, the amplitude value is determined by the expression defined in Eq. (1). This performs a post-processing pseudo-focusing of the full array aperture at each point in a discretised image region.

The Hilbert transform $\hat{u}(t)$ of the FMC dataset allows the computation of the analytic image. For each transmit tx and receive rx element pair in the system, the Hilbert transform of the corresponding A-Scan in the FMC dataset is selected. The amplitude value extracted from the Hilbert transform is selected based upon the time delay obtained from the ToF map, for both transmission and reception at pixel position (x_i, z_j) . The resulting pixel amplitude is the sum of amplitude values across each transmit-receive element pair.

$$I(x_i, z_j) = \sum_{tx=1}^{N_{tx}} \sum_{rx=1}^{N_{rx}} \hat{u}_{tx,rx}(\tau_{tx}(x_i, z_j) + \tau_{rx}(x_i, z_j)) \quad \text{Eq. (1)}$$

In this instance, the element vectors N_{tx} and N_{rx} are ‘view’ dependant. This assumes that N is a vector containing element numbers 1 to N_T , where N_T is the total number of active elements within the system. In this case, two 64-element arrays are used, and such $N_T = 128$. The element vector required for each view in this case is outlined in the following table.

The TFM algorithm was processed on a Graphics Processing Unit (GPU) using the MATLAB GPU Coder [26,27]. This creates optimised CUDA C++ code from a MATLAB function. This allowed imaging processing times to be reduced, with an average processing time of approximately 1s per 600x125 pixel TFM frame, using an NVIDIA Quadro T2000 graphics card.

2.5. Image mixing

To condense the number of images produced for analysis, views and modes can be mixed based on the information obtained to produce a single image. This is approached by first categorising images into three groups; (1) images which do not contribute to a defect response, (2) images which display a defect diffraction response, and (3) images which display a defect reflection response. In turn, two mixed images can be created: a diffraction response image I_D and a reflection response image I_R .

Diffraction effects across multiple images will be coherent in position, so are suitable to mix by a product method. By taking the product of each pixel across multiple images, we can exploit this positional coherence, while suppressing incoherent noise regions. A clear indication of the defect length, by way of top and bottom tip indications, should therefore be observed. This is achieved using the expression in Eq. (2), where I^d is a given TFM image which contributes to diffraction effects.

$$I_D = \prod_n^N I_n^d \quad \text{Eq. (2)}$$

Reflection indications, unlike diffraction effects, are not necessarily coherent across multiple images. This is due to the non-negligible width (1.0 mm) of the notch, as shown in Fig. 7. Therefore, a combined reflection image I_R is defined as the pixel-by-pixel sum of reflection contributing TFM images as defined in Eq. (3), for reflection contributing images I' . Similarly, to the diffraction image, this should give us an indication of the width of the defect.

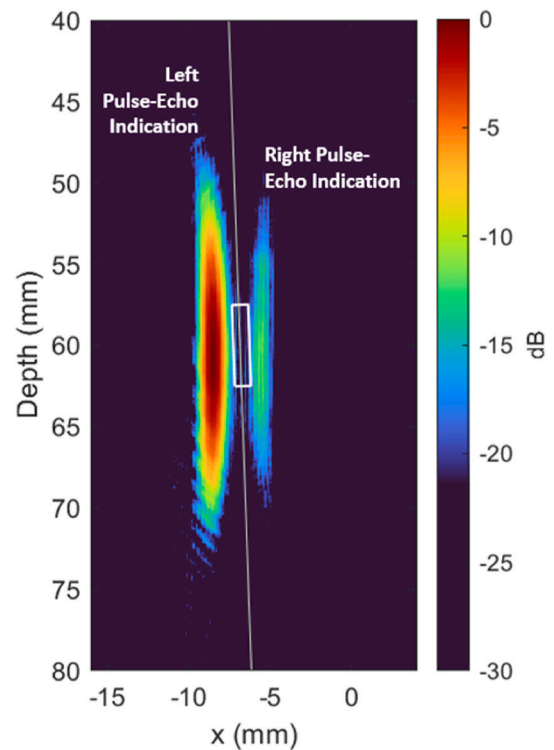


Fig. 7. Demonstration of incoherent reflections from each LL-T pulse-echo view in sample NG2.

$$I_R = \sum_n^N I_n' \quad \text{Eq. (3)}$$

The result of this is two images, each theoretically displaying the extent of the defect in each dimension in the image plane. By adding the two mixed images, a mixed image which shows the full extent of the defect can be created. This final mixed image I_T , defined in Eq. (4), is the sum of the two linearly normalised images for diffraction and reflection responses.

$$I_T = \hat{I}_D + \hat{I}_R \quad \text{Eq. (4)}$$

Normalisation before summation allows the relative amplitudes to be ignored, as diffraction effects are typically much lower in amplitude than reflected responses, and results in a superimposed image.

In this work, this process is done manually by observing each of the image modes and subsequently determining their relevant category. However, this requires prior knowledge of the defect location and geometry, as well as the human interpretation of images. Similar methods exist for completing this process automatically. One method is the matched filter approach for fusion of multi-mode TFM images in characterising crack-like defects [28,29]. Such methods can remove the requirement for prior defect knowledge, while providing statistical analysis of mixed modes to produce a single image showing the full extent of a defect. Additionally, a correlation approach for determining contributing modes has been demonstrated for near-vertical planar flat-bottom holes (FBHs) using multi-mode C-SAFT (TFM) method [16]. This has also been approached from a machine learning perspective, with the goal to improve performance and accuracy of multi-mode immersion imaging [30].

2.6. Image sensitivity calculations

The sensitivity of a given TFM image is quantified by its Signal-to-Noise Ratio (SNR). This value is defined as the logarithmic ratio of

maximum amplitude $A_{max}(I)$ and the Root Mean Square (RMS) of the noise level $A_{noise}(I)$ of the image domain I , as expressed in Eq. (5) [31].

$$SNR = 20 \log_{10} \left(\frac{A_{max}(I)}{\sqrt{\langle A_{noise}(I)^2 \rangle}} \right) \quad \text{Eq. (5)}$$

However, the generalisation of this value, by considering the maximum amplitude of the image, may not give an accurate reflection of the image sensitivity. For instance, artefacts such as wedge and backwall reflections may provide the highest amplitude and therefore falsify the apparent sensitivity of an image.

In this work, where the position and extent of flaws are known well, the SNR value is calculated based upon a defined region around the flaw. The maximum image amplitude is replaced with the maximum amplitude defined within this region r surrounding the known defect, ensuring that only defect indications are considered. Furthermore, the noise level can be defined in Eq. (6) as the RMS of the image noise solely excluding the defect indication $A_{noise}(I_n)$, where $I_n = \{I_n \in I, \sim (I_n \in \{r\})\}$.

$$SNR = 20 \log_{10} \left(\frac{A_{max}(r)}{\sqrt{\langle A_{noise}(I_n)^2 \rangle}} \right) \quad \text{Eq. (6)}$$

This method will be used to quantify the relative sensitivity between images. To retain an accurate relative sensitivity, comparisons can only be made where the image domain and defect regions are of the same area and pixel density.

3. Test samples

Three carbon steel samples were created to test the dual-tandem phased array setup, all with a height of 120 mm, length 500 mm and 35 mm depth. Each sample was cut from the same steel block, and as such consistent elastic properties were observed. The longitudinal velocity was determined to be 5930 ms^{-1} by considering backwall reflections through the sample depth, with the shear velocity approximated at 3240 ms^{-1} .

Each sample contained one EDM notch of dimensions 5.0 mm by 1.0 mm machined 10 mm into the sample face, machined along a mock narrow-groove weld face at a 2° rotation to the Z-axis, placed at depths of 27.5 mm, 60 mm and 92.5 mm, to positionally and geometrically represent expected LOSWF flaws throughout the full thickness of a narrow-groove weld. The three samples used in this work are shown in Fig. 8, presented in the X-Z image plane. The details of the EDM notch defects in the samples are shown in Table 3, in terms of x-position, z-position and rotation, relative to the centre of the EDM notches.

4. Probe Centre Separation

The separation between the centre of the two arrays, defined symmetrically at the centre of the weld, is a crucial consideration in terms of imaging sensitivity. A Probe Centre Separation (PCS) value must be

Table 3
Carbon steel samples defect positioning.

Ref. Name	Defect		
	X (mm)	Z (mm)	Θ ($^\circ$)
NG1	-7.9	27.5	2.0
NG2	-6.8	60.0	2.0
NG3	-5.6	92.5	2.0

carefully selected based upon a knowledge of the height of the weld sample, such that the full depth of the weld is covered by the array beam profiles. Assuring this ensures that only a single acquisition is necessary to observe potential flaws across the full weld height. A low PCS value will concentrate energy towards the sample surface, while reducing energy at the backwall. Conversely, a high PCS will reduce energy near the surface of the sample, as well as encourage energy loss with increased path lengths.

4.1. PCS study

A study to understand the sensitivity of images at different PCS values was conducted using the dual-tandem setup for each of the three mock narrow gap samples (NG1, NG2 & NG3), to ensure PCS sensitivity across the full height of the weld could be considered. The sensitivity values obtained in this study were calculated using the method discussed in Section 2.6. Three PCS values were chosen, such that the longitudinal normal beam of the two arrays intersected at a depth of 1/3 (167 mm), 1/2 (238 mm) and 2/3 (314 mm) of the sample thickness. A TFM image was created for each PCS value, using the dual-tandem FMC acquisition process discussed above. The sensitivity for each of the four 'views' was calculated for the modes presented in section 2.2, for each of the three PCS values in each sample.

The bar plot in Fig. 9 shows the mean sensitivity at each PCS for each mode, for each of the four views. A PCS corresponding to a longitudinal crossover of 2/3 sample thickness, showed the highest sensitivity across each of the pulse-echo modes, except LL-T and right L-L. The 1/3 thickness PCS exhibited the highest sensitivity for through-transmission. However, this was due to a strong reflection from the top of the lower notches, while exhibiting no diffraction effects. Therefore, it was decided that the ability to resolve diffractive effects – as part of the purpose of this work – was considered more valuable to this work.

Based upon these findings and given that all samples used in this work had a height of 120 mm, the 2/3 thickness PCS value of 314 mm was chosen to be the PCS value used throughout the remainder of the study.

4.2. PCS error study

To understand the precision levels required for array positioning, a PCS sensitivity study was conducted with added artificial errors. This considered a single FMC frame with a PCS of 314 mm, by adding a PCS error during the ray-tracing process. The artificial error was

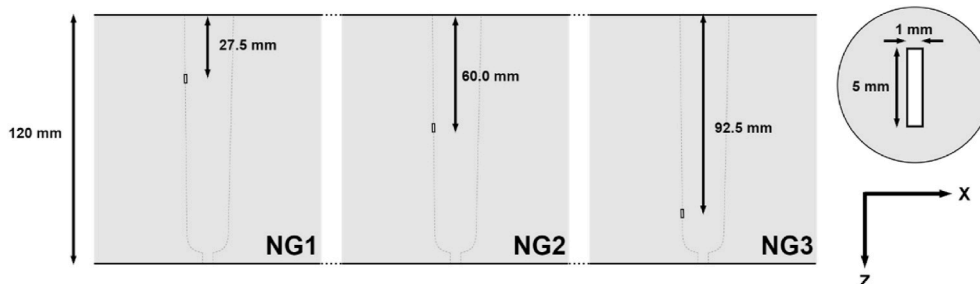


Fig. 8. EDM notches in carbon steel samples.

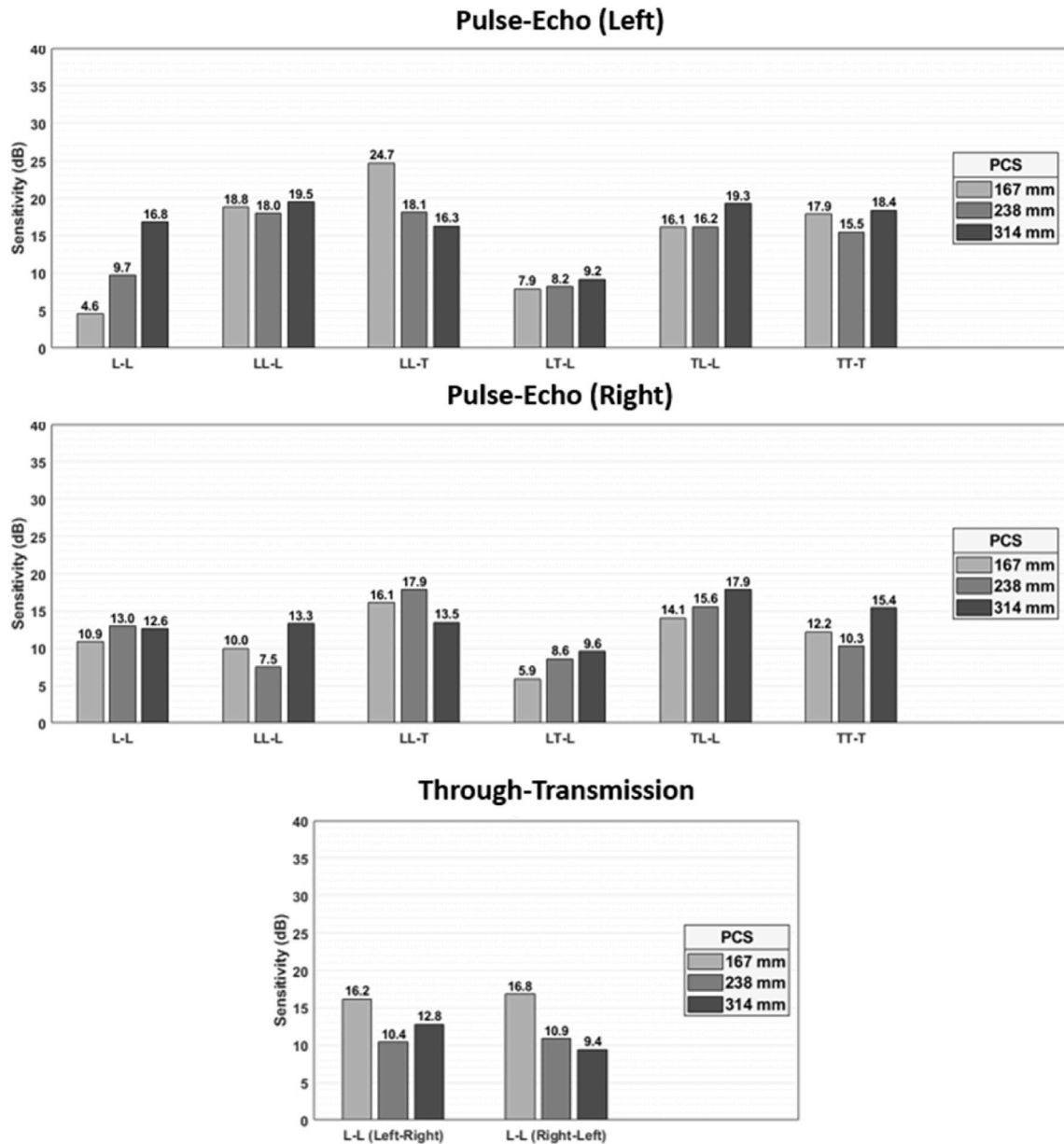


Fig. 9. PCS sensitivity study results for pulse-echo (left), pulse-echo (right) and through transmission.

incremented from -5 mm to $+5$ mm and applied to the true PCS value, with image sensitivity recorded for each view in each mock narrow-groove sample (NG1, NG2 & NG3). This error was applied to the PCS value, while maintaining a consistent centre point, as shown in Fig. 10.

As this is a linear offset, the error should not noticeably affect the synthetic focusing of pulse-echo views as this is dependent on a single array. Instead, this is expected to provide a positional error – shifting the defect position with respect to the ‘real’ position. Conversely, for the through-transmission views, focusing will be altered as the relative position of each array is considered in the delay law calculations.

The results of this study can be found in Fig. 11. It is clear that a positional error does affect the sensitivity of TFM images, and the effect is mode dependent.

This demonstrates that generally, the PCS does not affect the sensitivity more than ~ 3.0 dB at what is considered an extreme PCS positional error in this study. However, as previously stated, the effect of this error creates a purely positional error in pulse-echo images - equal to the positional error of the wedge position relative to the PCS centre point - as focusing is unchanged. It is the through-transmission imaging that is

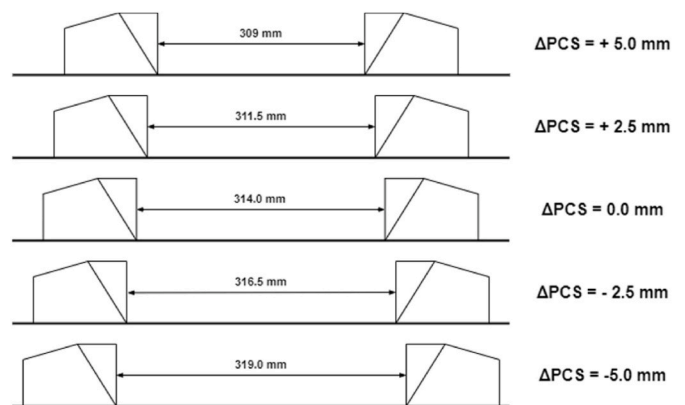


Fig. 10. PCS values used to study PCS error.

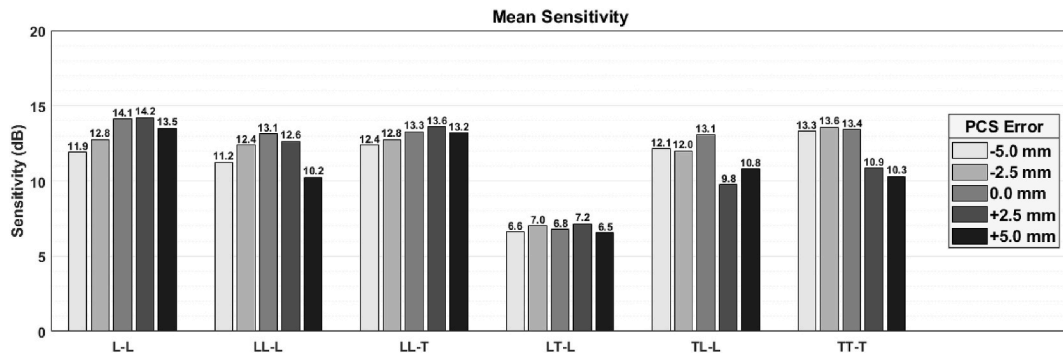


Fig. 11. PCS error effect on image sensitivity applied to 314 mm PCS.

likely to be impacted most by this error.

A final sensitivity analysis was conducted to understand the effect of PCS error on through-transmission focusing in TFM images using the direct longitudinal mode, L-L. The results of this are shown in Fig. 12.

It is clear from this study that, particularly at positive values, the sensitivity of through-transmission images is heavily dependent on PCS error. This asymmetrical sensitivity trend may be due to the encroachment of the lateral wave further into the image due to a positive positional error. In any case, this underlines the importance of precise PCS measurements when considering through-transmission imaging.

5. Mock narrow-groove samples

As previously discussed, mock narrow-groove samples NG1, NG2 & NG3 were designed to replicate LOSWF defects in a 2° narrow-gap J-groove. These were placed at depths of 27.5 mm, 60 mm and 92.5 mm respectively, relative to the notch centre. This section will firstly present TFM images obtained from a standard shear wave inspection, and then images generated using the dual-tandem method, with a PCS of 314 mm.

5.1. Shear inspection

To ensure a fair comparison and quantification of the improvement offered by the dual-tandem method, a standard shear inspection was conducted. An Olympus 36.1° Rexolite shear wedge (SA32-N55S-IHC) was used to observe the performance of a typical ultrasonic inspection of each of the three-mock narrow-groove samples. The Probe was positioned 100 mm from the sample centre, as a suitable trade-off between

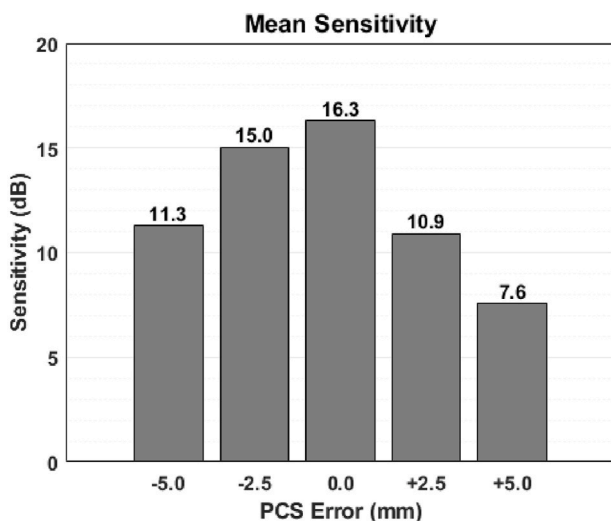


Fig. 12. PCS error mean-view sensitivity study for L-L through-transmission images.

required beam steering and path length.

A TFM image was obtained from each sample, using the self tandem shear mode TT-T. Fig. 13 (b) shows the TFM image of the sample containing a notch at half the sample thickness. There is a clear notch indication in this image, with relatively good sensitivity, although the height of the notch cannot be accurately quantified. However, Fig. 13 (a) and (c), where notches are present at 27.5 mm and 92.5 mm depths respectively, provide no obvious notch indications. This demonstrates the lack of weld coverage available using this method.

5.2. Pulse-echo

The following section discusses the pulse-echo imaging results obtained using the 20° wedge discussed previously for transmission of both shear and longitudinal waves. Fig. 14 shows the pulse-echo images from the left array, for each imaging mode in sample NG1. Two modes appear to show clear indications from the 27.5 mm deep 2° notch. The direct longitudinal mode L-L in Fig. 14 (a) displays the highest sensitivity to the notch, however it appears distorted due to the intensity of the beam steering required to reach the shallow depth. Conversely, the longitudinal self-tandem mode LL-L in Fig. 14 (b), provides the most accurate notch geometry, despite having a poorer SNR. The added backwall skip

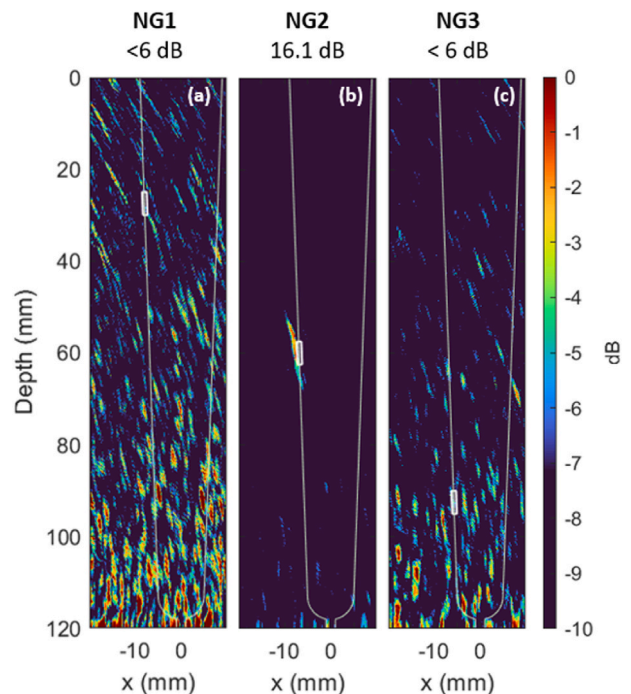


Fig. 13. TFM images of mock narrow-groove samples using self-tandem shear (TT-T) pulse-echo inspection with a shear-transmission optimised wedge.

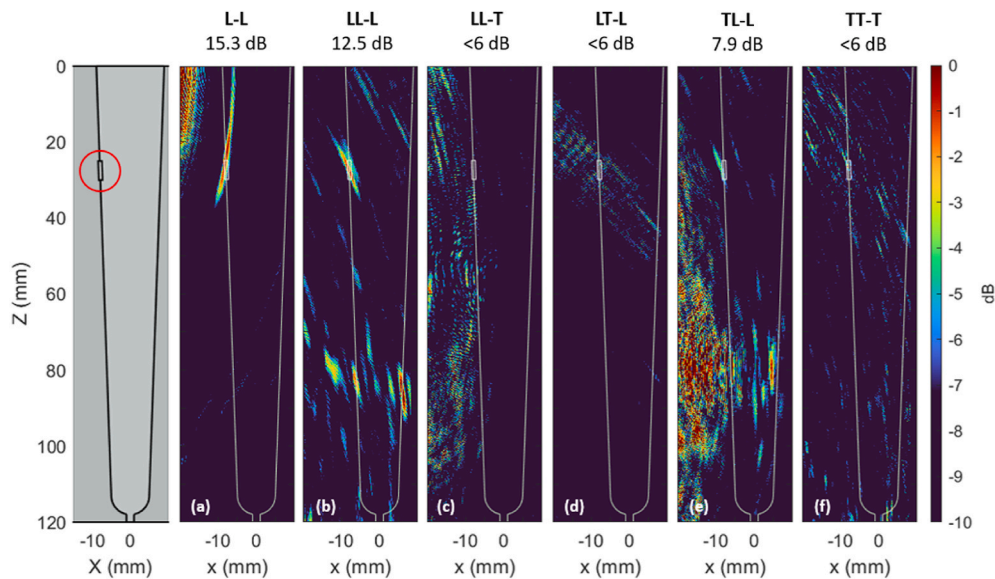


Fig. 14. Sample NG1, 27.5 mm notch depth multi-mode pulse-echo TFM.

demands less extreme steering for focusing at the shallower depth, relative to the direct longitudinal mode. However, the LL-L mode has several artefacts which could be mistaken for additional defects, and as such is likely to return several false-positives if considered in isolation. This is likely ‘leakage’ of another mode indication – which is something that must be considered when analysing multi-mode TFM images.

The remainder of the modes present no clear notch response, and as such exhibit low SNR values. Of these four in Fig. 14(c–f), the TL-L mode is the only one which shows a slight indication, however this cannot be confidently resolved from surrounding artefacts without prior knowledge.

In sample NG2, where the notch is located at half the sample thickness, all modes provide a greater sensitivity to the notch relative to sample NG1, as seen in Fig. 15. The LL-L mode in Fig. 15 (b) provides a high sensitivity indication of reflection from the notch, with no artefacts which could present a false-positive as seen with the shallow notch. The direct longitudinal mode L-L also exhibits top and bottom tip-diffraction, which allows the extent of the defect length to be obtained through geometric sizing methods. In addition, the LT-L mode in Fig. 15 (d)

provides tip diffraction, albeit with the poorest sensitivity. The remaining modes exhibit reflections from the notch face, with the LL-T mode providing the greatest sensitivity of the selected modes. Notably, the TT-T mode exhibits a higher SNR value than is seen in Fig. 13 (b), where a shear wedge is used.

Fig. 16 demonstrates the sensitivity of each mode to a notch at 92.5 mm depth, in sample NG3. Again, the L-L and LT-L modes, in Fig. 16 (a) and (d), exhibit tip diffraction effects, with the direct mode showing the best sensitivity to these effects. The shear mode TT-T provides the highest sensitivity to notch reflections observed across all samples, as seen in Fig. 16 (f). Furthermore, the LL-T and TL-L modes present additional second artefacts, which could be mistaken for a second notch and again risks a false-positive in isolation. This again highlights the caution required when considering multi-mode TFM. All but one (LT-L) of these modes provide a higher sensitivity value than the 16.1 dB value seen using the shear wedge in Fig. 13 (b), demonstrating the increased sensitivity to near-vertical defects obtained by using the optimised wedge angle.

The TFM images presented in this section have demonstrated the

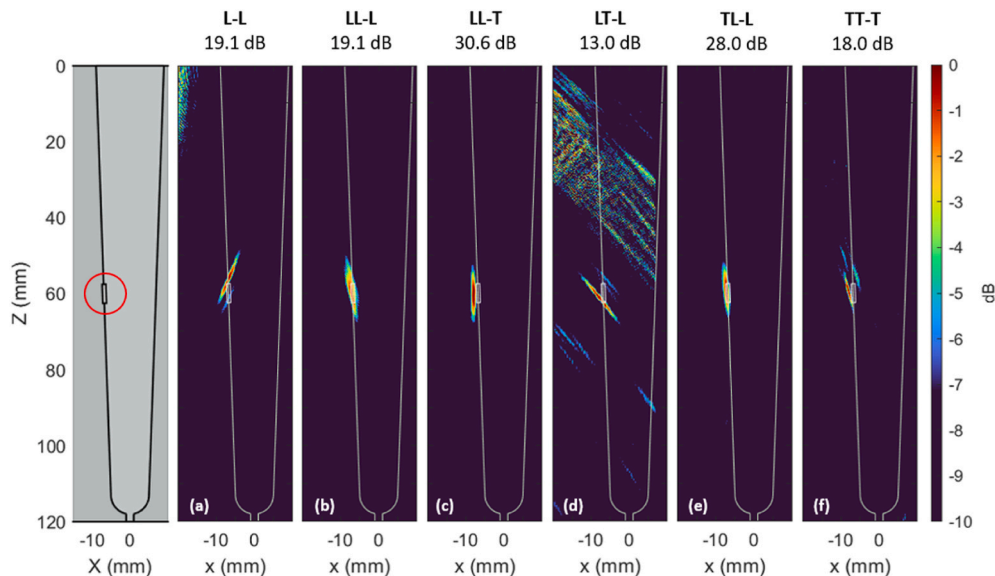


Fig. 15. Sample NG2, 60 mm notch depth multi-mode pulse-echo TFM.

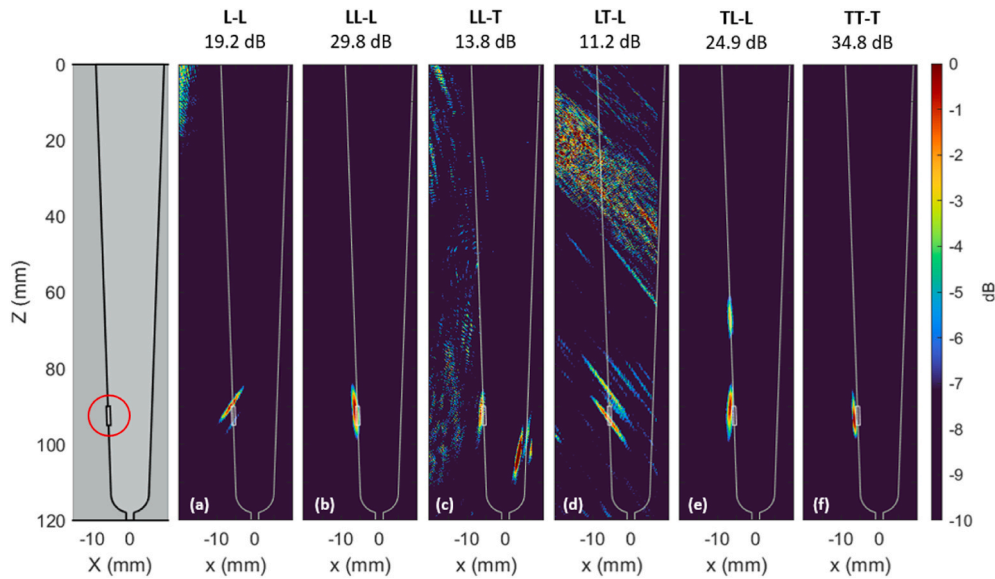


Fig. 16. Sample NG3, 92.5 mm notch depth multi-mode pulse-echo TFM.

capability of pulse-echo imaging for detection of near-vertical defects in a mock narrow gap sample, using multi-mode TFM. The sensitivity values of the images presented in this section are summarised in Table 4. Sensitivity has been shown to be greater for larger depths, where focusing requires less extreme beam steering. The shallow notch in sample NG1 is only visible in the L-L and LL-L modes, with relatively low sensitivity when compared with notches in samples NG2 and NG3. The shear and longitudinal self-tandem modes provide the best sensitivity at the deepest notch.

5.3. Through-transmission

Considering the L-L mode in through-transmission in Fig. 17, the lateral wave response is again observed. The dead zone due to this lateral wave masks the defect response from the shallow notch in NG1.

The notch at half the sample thickness in Fig. 17 (b) displays a strong bottom tip-diffraction. However, due to the directivity of the longitudinal beam, there is a large difference between this and the top tip-diffraction response. In turn, the top tip is lost in the colour scale, with an amplitude response 6.0 dB below the bottom tip. The peak-to-peak response displays a notch size of 6 mm.

In Fig. 17 (c), the deepest defect at 92.5 mm depth exhibits both top and bottom tip diffraction responses, with a peak-to-peak size of 5.5 mm.

5.4. Image mixing

Due to the large number of images produced using this method, interpretation can be arduous. In order to condense the acquired image information, an image mixing process is performed as discussed in section 2.4.

For each of the mock narrow-groove samples, a mixed image was formed based on interpretation of images and their indication of diffraction and reflection responses from the EDM notches. Based upon

Table 4
Summary of pulse-echo image sensitivity for mock narrow-groove samples.

Sample	Sensitivity (dB)					
	L-L	LL-L	LL-T	LT-L	TL-L	TT-T
NG1	15.3	12.5	< 6	< 6	7.9	< 6
NG2	19.1	19.1	30.6	13.0	28.0	18.0
NG3	19.2	29.8	13.8	11.2	24.9	34.8

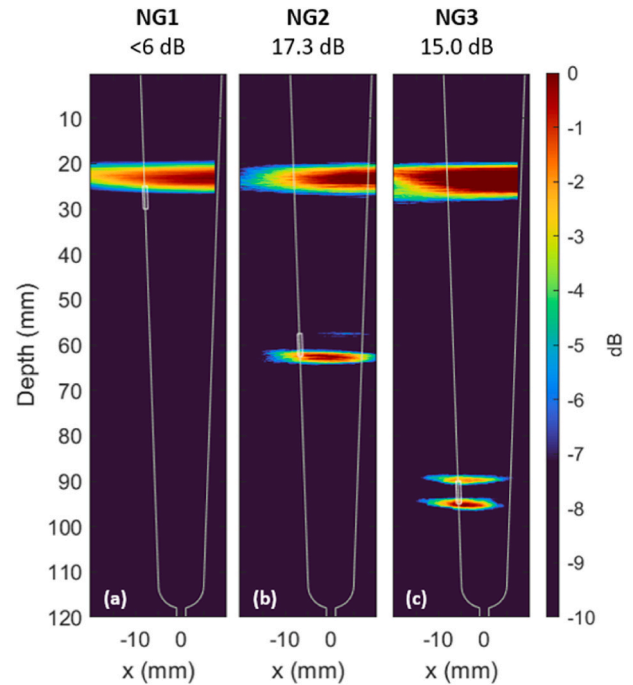


Fig. 17. Narrow-groove sample imaged at 314 mm PCS in through-transmission with mode L-L for samples (left) NG1, (middle) NG2 & (right) NG3.

this interpretation, it was determined that the L-L mode would form the fused diffraction image, by a pixel-by-pixel product of the pulse-echo and through-transmission images, as defined in Eq. (2). Furthermore, the pulse-echo images of modes LL-L, LL-T and TT-T were fused by pixel-by-pixel summation according to Eq. (3). These two images were then normalised and superimposed as defined in Eq. (4), to provide a single image. Fig. 18 shows the resulting mixed images for each of the mock narrow-groove samples. It should be noted that, although these images are presented on a logarithmic decibel scale, they do not represent relative amplitude values - due to the superimposing of two normalised images.

As the diffraction and reflection images are normalised prior to

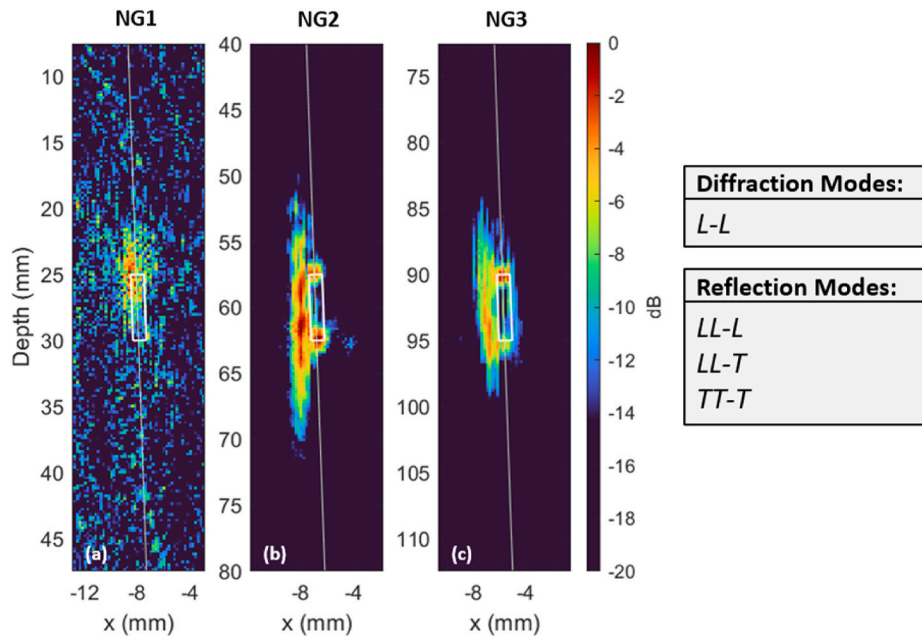


Fig. 18. Image mixing in mock narrow gap samples (a) NG1, (b) NG2, and (c) NG3 using diffraction modes L-L, and reflection modes LL-L, LL-T & TT-T.

mixing, a sensitivity value should not be calculated due to the post-normalisation superimposition of the diffraction and reflection images. Any attempt at such calculation of the final mixed image would provide a misleading and inaccurate result. Nonetheless, in Fig. 18 (b) and (c) - samples NG2 and NG3 - where the EDM notch is placed at a depth of 60 mm and 92.5 mm respectively, there is an indication of the geometric extent of the notch in both image axes.

6. Discussion

It has been shown that the dual-tandem phased array setup can provide greater coverage and sensitivity to thick-section, narrow-groove weld inspection. To further quantify the imaging performance, both the relative image amplitudes and defect sizing accuracy are considered. These will be discussed in the remainder of this section.

6.1. Relative amplitude

To understand the relative amplitudes between each mode in the

three-mock narrow-groove samples imaged in Section 5, both the maximum image amplitude and maximum notch amplitude were extracted. This allows the difference – if any – between the maximum image amplitude and maximum notch response amplitude to be observed. If the image and notch amplitude values are equal, it can be reasoned that the notch response is the maximum amplitude response within the image. A difference in these values suggests that an artefact other than the notch dominates the image.

Firstly, this was conducted for pulse-echo views only in samples NG1, NG2 and NG3 - the results of which are found in Fig. 19. Each bar is notated with an 'L' or 'R' to indicate a left or right pulse-echo view. Each view has a maximum image value shown as the wider bar, as well as the maximum notch amplitude by the thinner bar. By normalising these values to the maximum amplitude value across all images, a relative comparison can be made. In this case, values are normalised to the maximum image value of the left TT-T pulse-echo image in sample NG3, and all other values are displayed as a percentage of this amplitude value.

As the notch is offset from the centre of the sample to the left in this

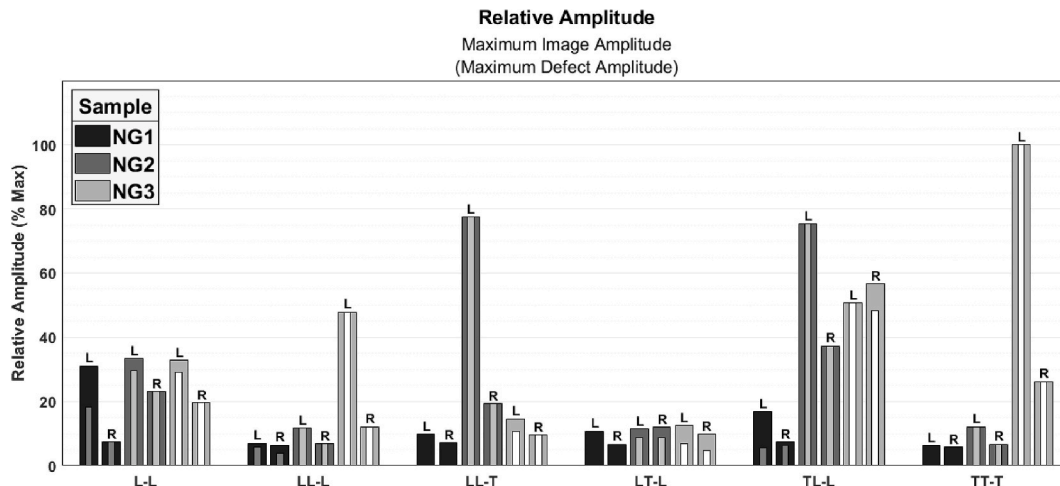


Fig. 19. Relative amplitude study of mock narrow-groove pulse-echo TFM images. Amplitudes are normalised to the maximum amplitude (NG3 left pulse-echo), with maximum image and defect amplitudes shown. Left pulse-echo views are noted by 'L' and right pulse-echo views by 'R'.

reference frame, there is a disparity in amplitude between left and right views, with the left pulse-echo view predominantly exhibiting higher notch response amplitudes. An inequality in the maximum amplitude value extracted from the notch and from the image as a whole, suggests that artefacts with high amplitude relative to the notch response are present in the image.

As observed in the TFM images above, some modes in sample NG1 do not provide any notch indications, so the notch amplitude is zero. Considering samples NG2 and NG3, with notch depths of 60 mm and 92.5 mm respectively, modes L-L and TL-L provide the most consistent notch sensitivity. Despite providing the highest notch amplitude response, the disparity between left and right TT-T views is notable due to the offset position of the notch relative to the PCS centre.

The same study can be conducted to observe the relative amplitudes of L-L pulse-echo and L-L through-transmission images, shown in Fig. 20. Again, the amplitude values are normalised to the same value as in Fig. 19.

As discussed previously, the L-L through-transmission images in sample NG1 do not provide notch responses, as these are likely masked by the lateral wave. In the through-transmission images of sample NG2 and NG3, it is seen that the notch response is approximately 5.0 dB below the maximum image amplitude. This suggests that the lateral wave response is often double the amplitude of that of the notch, quantifying the difficulty in imaging shallow flaws near the lateral wave response.

It is also noted that the maximum through-transmission image amplitude of sample NG1 is higher than that of the other two samples. As the notch response is masked by the lateral wave, this increase may be because by the summation of the notch and amplitude responses, even though they cannot be individually resolved in imaging.

The pulse-echo notch responses are higher in amplitude than through-transmission for samples NG2 & NG3 by an average of 8.8 dB for the right view and 11.0 dB for the left. This increase in relative amplitude for the left view is expected, as the notch is physically offset from the PCS centre in this direction, reducing the pulse-echo path relative to through-transmission.

6.2. Notch sizing

Typically, when sizing LOSWF defects with a pulse-echo phased array inspection methods, amplitude drop methods are employed - typically 6 dB, 12 dB or 20 dB [32]. The 6 dB drop case works on the assumption that once the maximum defect amplitude response drops to approximately 50% when the beam is focussed on the very edge of the

flaw. However, the accuracy of this method relies heavily on defect orientation and geometry, as an assumption of defect orthogonality to the ultrasonic beam must be made in this case of planar defects such as LOSWF.

The advantage of using longitudinal modes, particularly for through-transmission imaging, is the ability to observe tip diffraction effects. This provides accurate sizing of a planar defect's height, using the peak-to-peak distance between the top and bottom tips. As these indications are inherently caused at the extremities of a flaw, they provide more precise measurement capabilities than amplitude drop methods.

By utilising both the 6 dB amplitude drop method for reflective responses, and peak-to-peak method for diffraction indications, a mean notch size across each pulse-echo view was obtained for each mode and sample. Fig. 21 highlights the obtained notch height, with reference to the expected 5 mm height.

As is clear from the pulse-echo images presented previously, only the L-L and LL-L modes provided a resolvable defect response from the shallow notch in sample NG1. The L-L mode did not provide an accurate size, due to the spread of the notch response. However, the LL-L mode provided a height close to the expected 5 mm using the 6 dB drop method.

Considering the notch at half the sample thickness, in sample NG2, a notch height is determined for each mode. Modes L-L and LT-L provided tip-diffraction effects and had a 6.9 mm and 6.5 mm peak-to-peak notch height respectively. The TT-T mode 6 dB drop shows a 3.6 mm notch size. Despite having the lowest error of all modes in this sample, it is the only mode which under-sizes the notch. To ensure the safety of a scanned component, it is preferred to over-size rather than under-size flaws, and this result would therefore be a concern. The remaining modes, all using the 6 dB drop, oversize the notch height by at least 5 mm. Conversely, oversizing of a defect in this manner can be costly and can force unnecessary part rejection, or temporary operation shutdown. For this reason, it is important that defects can be accurately sized such that the appropriate action can be taken.

Now considering the deepest notch, in sample NG3, sizing was able to be conducted using each mode. Of the three notch depths considered, this provided the most accurate sizing across all modes. Again, modes L-L and LT-L provided tip diffraction indications, with the remaining modes showing reflections from the notch face. L-L and LT-L provided the most accurate notch height at 6.0 and 5.8 mm respectively. Modes LL-T and TT-T showed relatively accurate defect heights of 6.5 mm and 8.1 mm, with modes LL-L and TL-L greatly oversizing using the 6 dB drop method.

The same method can be applied to through-transmission imaging. In

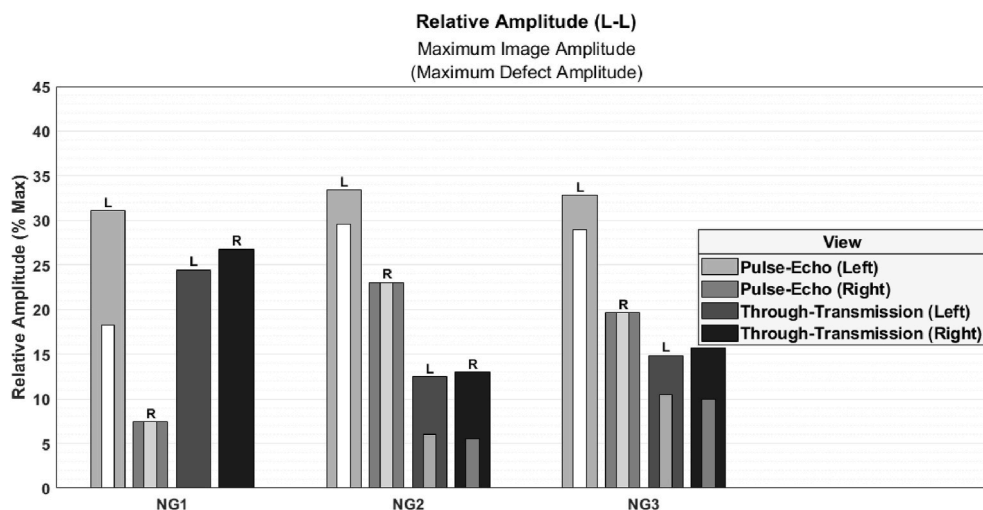


Fig. 20. Relative amplitude study of mock narrow-groove L-L TFM images. Amplitudes are normalised to the maximum amplitude (NG2 left pulse-echo), with maximum image and defect amplitudes shown.

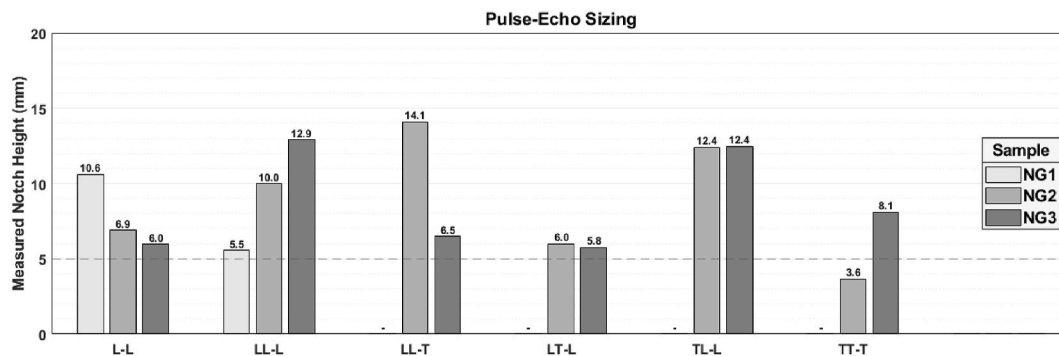


Fig. 21. Pulse-Echo sizing of notches in each mock narrow-groove sample. Peak-to-peak sizing method used for tip-diffraction indications, and 6 dB drop method for reflections.

this case, only diffraction effects are seen, so the peak-to-peak sizing method is used. Furthermore, only the direct longitudinal mode L-L is considered for through-transmission imaging.

It is initially obvious from Fig. 22 that the sizing error using through-transmission is reduced relative to the sizing conducted with pulse-echo. As discussed, the lateral wave masks the shallowest notch in sample NG1, therefore no defect response is present to allow sizing. Sample NG2 demonstrates a mean size across the through-transmission views of 6.1 mm. Furthermore, NG3 demonstrates a mean notch height of 5.0 mm. This follows the same pulse-echo trend for mode L-L, with increased sizing accuracy for deeper notches.

This demonstrates the ability to size the notch height in both pulse-echo and through-transmission imaging, with through-transmission improving the sizing error. However, due to the views available using this method, the width of the notch may also be sized. By considering the image mixing discussed previously, there is an opportunity to size the notch in both imaging axes. However, as discussed, this requires a great deal of operator input. Work is required to produce mixed images seen in Fig. 18 programmatically, such that the size can be extracted without the inclusion of human error.

In reality, defects such as LOSWF sized in this manner often have minimal width, so determining the width of the defect is not necessary. However, this method could be useful for other flaw types such as porosity and inclusions, to obtain a two-dimensional perception of the defect shape, without the requirement for amplitude drop methods.

It is clear that the dual-tandem method provides advantages to traditional shear pulse-echo in both detection and sizing of near-vertical defects in mock narrow-groove samples. The inclusion of pulse-echo acquisition from both weld sides allows each weld bevel to be imaged with equal sensitivity. Furthermore, the inclusion of longitudinal

through-transmission allows increased sensitivity to tip-diffraction effects. This has been shown to improve near-vertical notch sizing accuracy relative to pulse-echo methods.

7. Future work

The potential of the dual-tandem imaging method for imaging of near-vertical planar defects in mock narrow-gap samples has been shown in this work. Future work is focussed on the automated implementation of the dual-tandem method for inspection of narrow-groove welds in-process. This introduces added complexity both mechanically and ultrasonically and could require an adaptable PCS varied on a pass-by-pass basis. The use of Plane-Wave Imaging (PWI), which has been shown to provide comparative multi-mode imaging quality to TFM with a notable reduction in acquisition and processing times [33], may provide the possibility for a real-time implementation of the dual-tandem method.

In addition, the inspection of challenging (coarse-grained and anisotropic) materials may be suited to the increased diffraction sensitivity offered by the dual-tandem method. Furthermore, the optimisation of the acquisition and imaging processes could be improved by pre-inspection sensitivity mapping, allowing efficient mode selection and optimisation of the FMC acquisition method.

8. Conclusion

Traditional phased array weld inspection is conducted using a single probe in shear mode. However, this has proven to be ineffective when detecting and imaging near-vertical defects. In narrow-groove weld inspection, LOSWF defects present themselves along the bevel, at typically near-vertical angles. Furthermore, the thick-section nature of narrow-groove welding poses issues with increased attenuation and reduced full weld sensitivity. For this reason, the dual-tandem method is proposed to allow both pulse-echo and through-transmission detection of such defects.

An FMC acquisition and TFM imaging process which allows two pulse-echo and two through-transmission views to be obtained and imaged in a single scan. This was tested using three 120 mm thick carbon steel samples, with EDM notches placed in a position representative of a narrow-groove LOSWF defect at a varying sample depth. The resulting TFM images were found to show good sensitivity to near-vertical notches at various depths from both reflection and diffraction effects. Through-transmission imaging provided accurate notch sizing at deeper defects with high-quality TFM images. The introduction of an image mixing algorithm allowed the full extent of the defect in the image plane to be observed at lower notch depths.

Future work includes developing a sensitivity mapping algorithm for optimal mode choice, imaging of coarse-grain microstructures, and development towards an automated in-process inspection system.

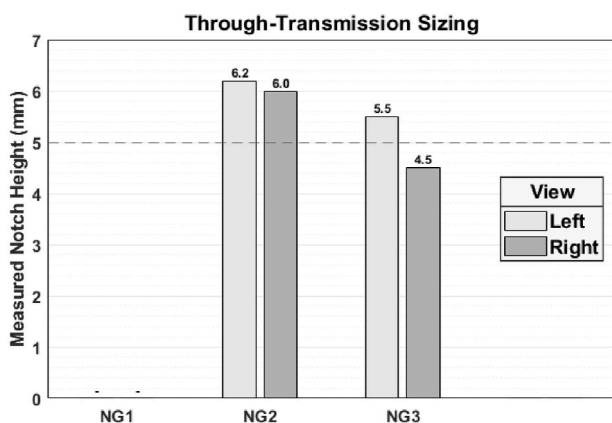


Fig. 22. Through-Transmission sizing of notches in each mock narrow-groove sample using peak-to-peak sizing method using L-L mode.

9. Author declarations

The authors have no conflicts to disclose.

Author statement

Ewan Nicolson: Conceptualization, methodology, software, data curation, writing, original draft preparation, reviewing and editing, **Charles MacLeod:** Supervision, reviewing and editing, methodology, **Ehsan Mohseni:** Supervision, reviewing and editing, methodology, **Sumana:** Supervision, reviewing, **Dave Lines:** Supervision, reviewing, software, **Gareth Pierce:** Supervision, reviewing.

Declaration of competing interest

The authors declare that they have no known competing financial interests or personal relationships that could have appeared to influence the work reported in this paper.

Data availability

Data will be made available on request.

Acknowledgements

This work is supported by EPSRC Centre for Doctoral Training in Future Innovation in Non-Destructive evaluation (FIND) under EPSRC Grant No. EP/S023275/1.

References

- [1] Drinkwater BW, Wilcox PD. Ultrasonic arrays for non-destructive evaluation: a review. *NDT E Int* 2006;39(7):525–41.
- [2] Schmerr Jr LW. In: Schmerr Jr LW, editor. *Fundamentals of ultrasonic phased arrays*. Cham: Springer International Publishing; 2015.
- [3] Javadi Y, et al. Intentional weld defect process: from manufacturing by robotic welding machine to inspection using TFM phased array. 2019 [Author(s)].
- [4] Honarvar F, Varvani-Farahani A. A review of ultrasonic testing applications in additive manufacturing: defect evaluation, material characterization, and process control. *Ultrasonics* 2020;108:106227.
- [5] Zimmermann R, et al. Multi-layer ultrasonic imaging of as-built wire + arc additive manufactured components. *Addit Manuf* 2021;48:102398.
- [6] Taheri H, Hassen AA. Nondestructive ultrasonic inspection of composite materials: a comparative advantage of phased array ultrasonic. *Appl Sci* 2019;9(8):1628.
- [7] Stratoudaki T, Clark M, Wilcox PD. Laser induced ultrasonic phased array using full matrix capture data acquisition and total focusing method. *Opt Express* 2016;24(19):21921.
- [8] Fan C, et al. A comparison between ultrasonic array beamforming and super resolution imaging algorithms for non-destructive evaluation. *Ultrasonics* 2014;54(7):1842–50.
- [9] Hunter AJ, Drinkwater BW, Wilcox PD. The wavenumber algorithm for full-matrix imaging using an ultrasonic array. *IEEE Trans Ultrason Ferroelectrics Freq Control* 2008;55(11):2450–62.
- [10] Camacho J, Parrilla M, Fritsch C. Phase coherence imaging. *IEEE Trans Ultrason Ferroelectrics Freq Control* 2009;56(5):958–74.
- [11] Portzgen N, Gisolf D, Blacquiere G. Inverse wave field extrapolation: a different NDI approach to imaging defects. *IEEE Trans Ultrason Ferroelectrics Freq Control* 2007;54(1):118–27.
- [12] Holmes C, Drinkwater BW, Wilcox PD. Post-processing of the full matrix of ultrasonic transmit–receive array data for non-destructive evaluation. *NDT E Int* 2005;38(8):701–11.
- [13] Zhang J, et al. Defect detection using ultrasonic arrays: the multi-mode total focusing method. *NDT E Int* 2010;43(2):123–33.
- [14] Holmes C, Drinkwater BW, Wilcox PD. Advanced post-processing for scanned ultrasonic arrays: application to defect detection and classification in non-destructive evaluation. *Ultrasonics* 2008;48(6–7):636–42.
- [15] British Standards Institute. European committee for standardisation, and international organisation for standardisation. Non-destructive testing of welds – Ultrasonic testing – Use of automated phased array technology (ISO 13588:2019), in *Testing Levels*; 2-4.
- [16] Bazulin AE, et al. Reconstructing the image of reflectors at base-metal–weld interface using ultrasonic antenna arrays. *Russ J Nondestr Test* 2021;57(9):739–52.
- [17] Vithanage RKW, et al. A phased array ultrasound roller probe for automated in-process/interpass inspection of multipass welds. *IEEE Trans Ind Electron* 2021;68(12):12781–90.
- [18] Mohseni E, et al. Model-assisted ultrasonic calibration using intentionally embedded defects for in-process weld inspection. *Mater Des* 2021;198:109330.
- [19] National Instruments. LabVIEW v17. 2017. 64-bit.
- [20] Paul Wilcox. MFMC format. 2:[Available from: <https://github.com/ndtatbristol/mfmc>; 2019.
- [21] Mineo C, Lines D, Cerniglia D. Generalised bisection method for optimum ultrasonic ray tracing and focusing in multi-layered structures. *Ultrasonics* 2021;111:106330.
- [22] Mineo C, Cerniglia D, Mohseni E. Solving ultrasonic ray tracing in parts with multiple material layers through Root-Finding methods. *Ultrasonics* 2022;124:106747.
- [23] Sethian JA. Fast marching methods. *SIAM Rev* 1999;41(2):199–235.
- [24] Tant KMM, et al. A transdimensional Bayesian approach to ultrasonic travel-time tomography for non-destructive testing. *Inverse Probl* 2018;34(9):095002.
- [25] Hassouna MS, Farag AA. MultiStencils Fast marching methods: a highly accurate solution to the eikonal equation on cartesian domains. *IEEE Trans Pattern Anal Mach Intell* 2007;29(9):1563–74.
- [26] MathWorks. Matlab. 2022.
- [27] MathWorks. GPU coder. 2022.
- [28] Bevan RLT, et al. Data fusion of multiview ultrasonic imaging for characterization of large defects. *IEEE Trans Ultrason Ferroelectrics Freq Control* 2020;67(11):2387–401.
- [29] Wilcox PD, et al. Fusion of multi-view ultrasonic data for increased detection performance in non-destructive evaluation. *Proc Math Phys Eng Sci* 2020;476(2243):20200086.
- [30] Bevan RLT, Croxford AJ. Automated detection and characterisation of defects from multiview ultrasonic imaging. *NDT E Int* 2022;128:102628.
- [31] Villaverde EL, Robert S, Prada C. High-frequency Total Focusing Method (TFM) imaging in strongly attenuating materials with the decomposition of the time reversal operator associated with orthogonal coded excitations. 2017 [Author(s)].
- [32] Felice MV, Fan Z. Sizing of flaws using ultrasonic bulk wave testing: a review. *Ultrasonics* 2018;88:26–42.
- [33] Le Jeune L, et al. Plane Wave Imaging for ultrasonic non-destructive testing: generalization to multimodal imaging. *Ultrasonics* 2016;64:128–38.